Local Hydrogen Fluxes Correlated to Microstructural Features of a Corroding Sand Cast AM50 Magnesium Alloy

Philippe Dauphin-Ducharme,[a] R. Matthew Asmussen,[b] Ushula M. Tefashe,[a] Mohsen Danaie,[c] W. Jeffrey Binns,[b] Pellumb Jakupi,[b] Gianluigi A. Botton,[c,z] David W. Shoesmith,[b,*,z] and Janine Mauzeroll[a,,z]**

[a]*Laboratory for Electrochemical Reactive Imaging and Detection of Biological Systems, McGill University, Montreal, Quebec H3A 0B8, Canada*
[b]*Department of Chemistry and Surface Science Western, Western University, London, Ontario N6A 5B7, Canada*
[c]*Department of Materials Science and Engineering, Brockhouse Institute for Materials Research and Canadian Centre for Electron Microscopy, McMaster University, Hamilton, Ontario L8S 4M1, Canada*

Successful in situ spatiotemporal tracking of corrosion processes occurring at heterogeneous Mg alloy microstructures was achieved through tandem analyses involving electron and electrochemical microscopies. Through cross-correlation of scanning electron microscopy and scanning electrochemical microscopy images and subsequent analytical transmission electron microscopy, the morphology and chemical composition of microstructural components on the surface of a sand-cast AM50 Mg alloy were related to their respective local evolution of H_2 with micron scale resolution prior to, during and post corrosion. The results confirm that the preferential water reduction sites in the initial stages of corrosion are the Al_8Mn_5 intermetallics while a β-$Mg_{17}Al_{12}$ precipitate contaminated with Ni becomes cathodically active at a later stage of corrosion. This approach demonstrates the power of correlative approaches to probe and understand local electrochemical phenomena.
 [DOI: 10.1149/2.0571412jes] All rights reserved.

Manuscript submitted July 21, 2014; revised manuscript received August 19, 2014. Published August 30, 2014.

Owing to their light weight, high strength-to-weight ratio, good castability and high damping capacity, Mg alloys are ideal candidates for automotive structural components.[1–5] The compromise of formability, room temperature ductility and price represent major challenges in commercializing these materials. Importantly, Mg alloys also suffer from poor corrosion resistance in aqueous environments[6–8] and due to their positions in the electrochemical activity series, are highly susceptible to accelerated corrosion rates when in galvanic contact with a more noble material.[9] At open circuit, the overall galvanic current is null due to a balance between the anodic and cathodic current densities, while on a microscopic scale, a difference in electrochemical potential is obtained. In Mg alloys, galvanic coupling between microstructural components of the alloy (commonly referred to as microgalvanic coupling) stems from an inherent electrochemical potential difference between the Mg matrix and its secondary phases,[10–12] and can be tracked using local scanning probe methods.

Local scanning probe techniques such as several modes of scanning electrochemical microscopy (SECM),[13–19] scanning Kelvin probe force microscopy (SKPFM),[20–22] the scanning vibrating electrode technique (SVET)[23–25] and local electrochemical impedance spectroscopy (LEIS)[26] have been used to probe the heterogeneous surfaces of Mg alloys and to assess the electrochemical behavior of the different microstructural constituents responsible for microgalvanic corrosion. Among these techniques, SECM has the ability to quantify electrochemical fluxes in situ with high lateral resolution using a microelectrode (ME).[27] This technique has been successfully applied in corrosion research to provide in situ analyses of pitting corrosion at oxide films,[28–30] to assess lateral variations in corrosion kinetics,[31] and to detect defects within coated metal samples.[32]

The feedback mode of SECM has been employed to probe corroding AM60[15] and AZ31[17] Mg alloys. The increased feedback current was ascribed to a loss of the protective MgO film at specific locations.[15,17] The potentiometric mode of SECM has also been extensively employed to characterize both pHs and Mg^{2+} flux during corrosion of Mg alloys.[16,18,33–35] Lamaka et al. monitored both pHs and Mg^{2+} ions fluxes in situ over scratched surface and correlated the ionic fluxes to their respective galvanic roles using SVET.[18] Both Mg^{2+} and OH^- fluxes are of interest to understand the overall corrosion mechanism (summarized below) of Mg and its alloys.[36]

$$Mg_{(s)} \rightarrow Mg^{2+}{}_{(aq)} + 2e^- \quad [1]$$

$$2H_2O_{(aq)} + 2e^- \leftrightarrows 2OH^-{}_{(aq)} + H_{2(aq+g)} \quad [2]$$

$$Mg^{2+}{}_{(aq)} + 2OH^-{}_{(aq)} \leftrightarrows Mg(OH)_{2(s)} \quad [3]$$

The Mg^{2+} is generated by anodic oxidation of the matrix phase (Equation 1) while the reduction of water occurs predominantly on the more noble alloy constituents (secondary phases) producing dissolved molecular H_2 and OH^- species (Equation 2). Generation of OH^- in the cathodic reaction leads to localized pH changes and the deposition of $Mg(OH)_2$ (Equation 3) on the alloy surface ($K_{sp,}$ $Mg(OH)_2 = 5.61 \times 10^{-12}$).[37]

Recently, the substrate-generation/tip-collection (SG/TC) methodology using dissolved H_2 as a redox mediator was used to study the corrosion behavior of Mn,[38] Fe-3 at% Si alloys[39] and Mg alloys.[17,40] The comparison of probe approach curves recorded over the same location of a corroding AM50 Mg alloy with a numerical model, allowed the H_2 flux to be extracted.[40] The active site size and H_2 fluxes were also shown to be varying with immersion time when performing three-dimensional scans.[40] However, no direct cross-correlation between the molecular H_2 fluxes observed during the in situ SECM and microstructural features of the Mg alloy was reported. To elucidate the microgalvanic roles of these microstructural components and to correlate their morphologies and elemental compositions with their local reactivity, tandem electron and electrochemical microscopic imaging is required. This is in line with successful SECM methodologies reported on pure Zr, a material of interest for nuclear waste containers due to its high corrosion resistance.[41]

Building on our previous work,[40] spatiotemporal tracking of the local flux of dissolved molecular H_2 produced from a corroding AM50 Mg alloy has been measured by SECM in the SG/TC mode, and the microstructural features responsible for the generation of high H_2 fluxes identified by performing 3D SECM imaging on a pre-mapped area of the alloy. The areas responsible for high H_2 fluxes were then assessed by confocal laser scanning microscopy (CLSM) and transmission electron microscopy (TEM). The methodology presented herein enables the areas imaged ex situ, pre and post corrosion, to be superimposed with in situ electrochemical maps with high spatial

*Electrochemical Society Fellow.
**Electrochemical Society Active Member.
zE-mail: gbotton@mcmaster.ca; dwshoesm@uwo.ca; janine.mauzeroll@mcgill.ca

resolution. The development of such tandem microscopy methodologies is essential if SECM is to be quantitatively applied to examine the local corrosion of Mg alloys and to evaluate the potential of corrosion protection strategies.

Experimental

Sample preparation.— Sand cast AM50 Mg alloys, received as rods from General Motors Canada, were machined into 1 cm × 1 cm × 0.7 cm samples. The samples were then fixed in a cold mounting epoxy (Epofix – Struers), and then ground using SiC paper (800, 1200, 2400 grit). Finally, a mirror finish was produced using a 3 μm diamond paste (Dia3, Struers) with a Struers MD Dur cloth followed by a slurry of ethylene glycol and 0.04 μm colloidal silica (1:1 mixture) on a Struers MD Chem cloth for 2 min.[23] After aggregated silica was removed using sonication in anhydrous ethanol for 2 min, the sample was dried in an Ar stream.

Instrumentation.— The surface of the AM50 sample was imaged at 150×magnification across the entire 1 cm × 1 cm polished surface using a Hitachi SU6600 Field Emission scanning electron microscope (SEM). The images were then stitched using Image-Pro Plus 7.0 into a grid to yield a final image map of the entire surface (Figure 2A). Following immersion, the sample was imaged with a Hitachi 4500-N SEM equipped with a Quartz One energy dispersive X-ray spectroscopy (XEDS) System. Topographical analysis of the sample was performed with a Zeiss 510 confocal HeNe (633 nm) laser by detecting the reflected light intensity normalized in terms of known distance steps (slices) through the focal plane in order to reach the deepest region. By placing the sample downward on the microscope stage, normalized intensities can then be converted into distances.

SECM was performed with an ElProScan 3 system (HEKA, Germany; bipotentiostat model PG340) by positioning a 25 μm Pt ME, fabricated following an established protocol, over the immersed Mg alloy surface.[42] A 1 mM $Ru(NH_3)_6Cl_3$ (Acros Organic, New Jersey, USA) with 0.016 wt% NaCl (ACP, Montreal, Quebec) aqueous solution (Millipore MilliQ water 18.2 MΩ) was used to probe the surface corrosion behavior. The ME was positioned 10 μm from the surface using a feedback approach curve and then rastered across the surface at 5 μm/s while polarizing the ME at −100 mV. To perform a correlation of the SECM map with the SEM micrograph, identification of epoxy-Mg alloy edges were performed by recording line scans and maintaining a tip-to-substrate distance of 10 μm with the ME polarized at −100 mV. This allowed the determination of sample orientation and ME position. A Pt counter electrode (0.5 mm diameter, as drawn 99.99%, Goodfellow Cambridge Limited Huntingdon, England) and an Ag|AgCl reference electrode wire (1.0 mm diameter, annealed 99.99% Ag wire, Goodfellow), prepared following a literature procedure,[43] were employed to record electrochemical data. Following surface imaging by SECM, the sample was removed from the solution and washed thoroughly with ethanol.

A focused ion beam (FIB-Zeiss NVision 40, equipped with an XEDS- Oxford, Inca, Silicon drift detector) was used to prepare samples for TEM analysis from the identified locations on the surface. Microscopic characterization of the FIB samples was performed on an FEI Titan 80–300 (scanning) transmission electron microscope, (S)TEM, equipped with an XEDS (XEDS- Oxford, Inca, Si(Li) detector). Details regarding the electron microscopy and spectroscopy techniques applied can be found in a recently published study.[44] Samples were cooled to 95 K during microscopy observations to minimize beam-induced degradation.

Results and Discussion

In this study, the AM50 Mg alloy has been investigated due to its direct commercial application in the automotive industry.[45] The microstructure of the AM50 alloy is comprised of primary α-Mg matrix, eutectic α-phase with higher Al content than the matrix, and secondary phases: β-phase ($Mg_{17}Al_{12}$), and Al-Mn intermetallics (usually Al_8Mn_5, based on the AM50 phase diagram and previous experimental observations).[44]

From SKPFM[46] and galvanic coupling[47] studies, the α-Mg phase has long been reported to be less noble than the secondary phases and will preferentially dissolve (Equation 1). The β-phase has been reported previously to have a dichotomous role.[10–12] The latter can function as a microgalvanically-coupled cathode supporting water reduction (to H_2) in Al-containing Mg alloys (Equation 2) and as a physical barrier providing corrosion resistance.[10–12] Various Al-Mn intermetallics have also been reported as cathodic sites driving the corrosion process.[22,48,49]

Establishing which of the two secondary phases, Al-Mn intermetallics or β-phases, behaves as a preferential site for water reduction remains to be clarified. One study reported Al-Mn intermetallics to have a more positive corrosion potential than the β-phase inferring their prime cathodic behavior, although higher galvanic coupling currents were observed between the β-phase and representative α-Mg materials.[47] SKPFM, on the other hand, indicates the Al_8Mn_5 intermetallics are better cathodes.[46] These findings are based on ex situ analyses, involving galvanic current measurements and the consideration of Volta potentials, and lack local in situ identification of cathodic activity of the secondary phases.

SECM detection of local H_2 fluxes.— To characterize the microgalvanic roles of these three microstructural components, the

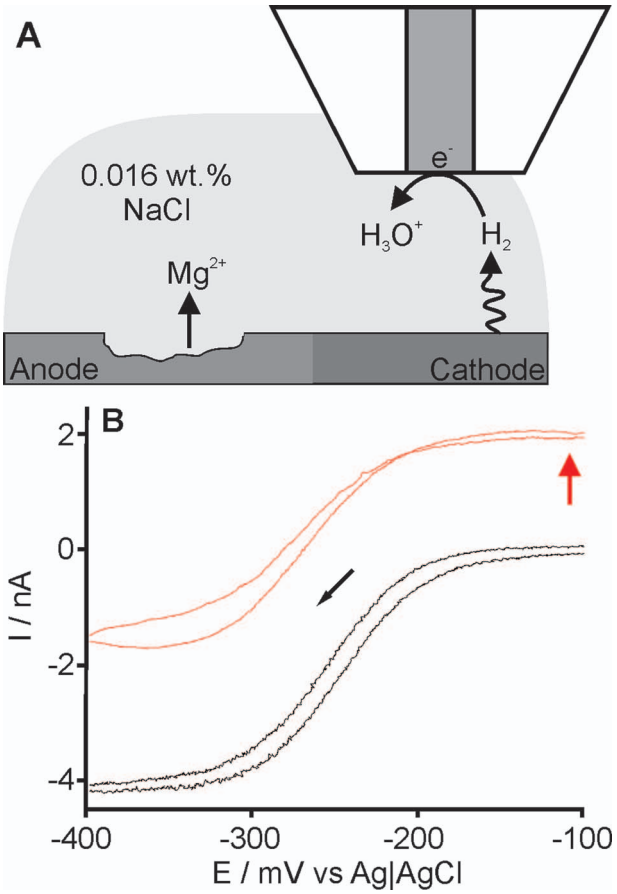

Figure 1. A) Schematic illustration of the microgalvanic corrosion mechanism on a Mg alloy and the use of SECM to detect the H_2 generated by collection at the ME tip. B) Cyclic voltammogram recorded on a 25 μm ME, located above an AM50 alloy, at 10 mV/s in a freely aerated 1 mM $Ru(NH_3)_6Cl_3$ (red curve) and 1 mM $Ru(NH_3)_6Cl_3$ + 0.016 wt% NaCl solution (black curve). The red arrow indicates the potential selected to perform the SECM scans. Counter electrode: Pt; reference electrode Ag|AgCl.

SG/TC mode of SECM can be employed, as illustrated in Figure 1A. During the initial stages of corrosion, the cathodic microstructural features will generate dissolved H_2, which can be oxidized at the ME, resulting in a faradaic current. Initially, when the Mg alloy is immersed in a salt solution (0.016 wt%), no dissolved H_2 is detectable. Figure 1B shows two voltammograms recorded at 10 mV/s in a 1 mM $Ru(NH_3)_6Cl_3$ solution prior to (black curve, with $E_{1/2} = -0.25$ V vs Ag|AgCl), and following exposure to the Mg alloy (red curve) in the bulk solution (tip-to-substrate distance > 300 μm). As can be seen, the steady-state response obtained at potentials > −200 mV can be attributed to the oxidation of dissolved H_2 at the Pt ME not present in the solution unexposed to the alloy (black curve). At less noble potentials (< −250 mV) the current response can be assigned to the reduction of the redox mediator ($Ru(NH_3)_6Cl_3$) in the solution. $Ru(NH_3)_6Cl_2$ can represent a potential parasitic source of faradaic current at potentials > −200 mV where the mediator solution ($Ru(NH_3)_6Cl_3$) reacts with the Mg alloy. However, no variation in the steady-state response recorded at < –200 mV, implying a change of [$Ru(NH_3)_6Cl_3$], was recorded. The H_2 produced during corrosion can, thus, be used as surface reactivity probe. By applying an anodic bias of –100 mV vs Ag/AgCl, denoted with a red arrow in Figure 1B, the ME "collected" the dissolved H_2 with negligible faradaic current contribution from [$Ru(NH_3)_6Cl_3$] reduction. The biased tip was then rastered across the heterogeneous Mg alloy surface to identify regions generating high H_2 fluxes.

To identify the microstructural features responsible for the generation of H_2, a polished 1 cm × 1 cm AM50 alloy was montage imaged with SEM prior to corrosion and is presented in Figure 2A. This procedure provided a fully mapped surface revealing the locations of the secondary microstructural features, β-phase and Al_8Mn_5 intermetallics, allowing the selection of an area of interest (AOI). Two AOI's, highlighted in Figure 2B, were selected for SECM imaging. Two Al_8Mn_5 intermetallic phases are marked with red and green arrows, and three β-phase particles with orange, blue and white arrows.

Rapid feedback current probe approach curves (less than 5 min after immersion) performed with the redox mediator, $Ru(NH_3)_6Cl_3$, ($E_T = -350$ mV vs Ag|AgCl) allowed the ME to be positioned 10 μm from the Mg alloy surface. After 30 min of immersion, SECM mapping was performed on AOI-1, which is displayed in the SEM image, Figure 3A. The resulting SECM map of AOI-1 (200 μm × 200 μm), recorded at a scan rate of 5 μm/s is presented in Figure 3B. Two regions of higher current, indicating higher H_2 flux, were observed. The dimensions of the regions responsible for the high H_2 fluxes were on the order of 5–10 μm, and corresponded to the locations of the Al_8Mn_5 intermetallic particles marked with the red and green arrows in Figure 3A. A second scan of AOI-1 was performed after 2 h of immersion and the resulting map is shown in Figure 3C. The two regions of high H_2 flux grew to approximately 20–25 μm in size and several new locations generating measureable fluxes appeared. The measured background current in Figure 3B and 3C remained constant, a sign that the reduction of $Ru(NH_3)_6Cl_3$ at the Mg surface was negligible.

AOI-2 (Figure 2B), was next imaged following a 4 h exposure period, Figure 3D. Approximately half of the 200 μm × 200 μm area mapped appeared to produce H_2. Again, locations on the order of 20–25 μm were observed to produce higher H_2 fluxes. The increase in the active site size responsible for producing H_2 is consistent with previously reported observations showing the rapid time dependency of Mg alloy corrosion.[40]

Correlation of the SECM and SEM maps.— Subsequent to the SECM measurements, the AOI's were characterized by SEM and CLSM. The SEM micrograph in Figure 3E displays AOI-1 following 6 h of immersion, and is superimposed with the SECM map (Figure 3C). This superimposition shows that the large H_2 fluxes detected coincided with the locations of the Al_8Mn_5 intermetallics. The β-phase location, indicated by the white arrow in Figure 3E, was producing only small amounts of H_2 after 2 h of exposure. Figure 3F shows an SEM image of the two AOIs mapped by SECM after the 6 h exposure period. The observed accumulation of domes of corrosion product on the microstructural features marked with arrows was expected from areas evolving H_2 due to the alkalinity produced (Equation 2) causing the precipitation of the Mg^{2+} generated at adjacent anodic sites (Equation 1).[18,50] The presence of such a dome at the β-phase location, indicated by the white arrow, suggests this cathodic location was activated during the 4 h exposure period after the recording of the map in Figure 3C (recorded after only 2 h). Two possibilities exist for the increase in active site size detected in SECM: (1) the development of a smaller tip-to-substrate distance due to protrusion of the accumulating dome of corrosion product above the high H_2 flux regions; (2) increased radial diffusion of H_2 from the cathodic site.

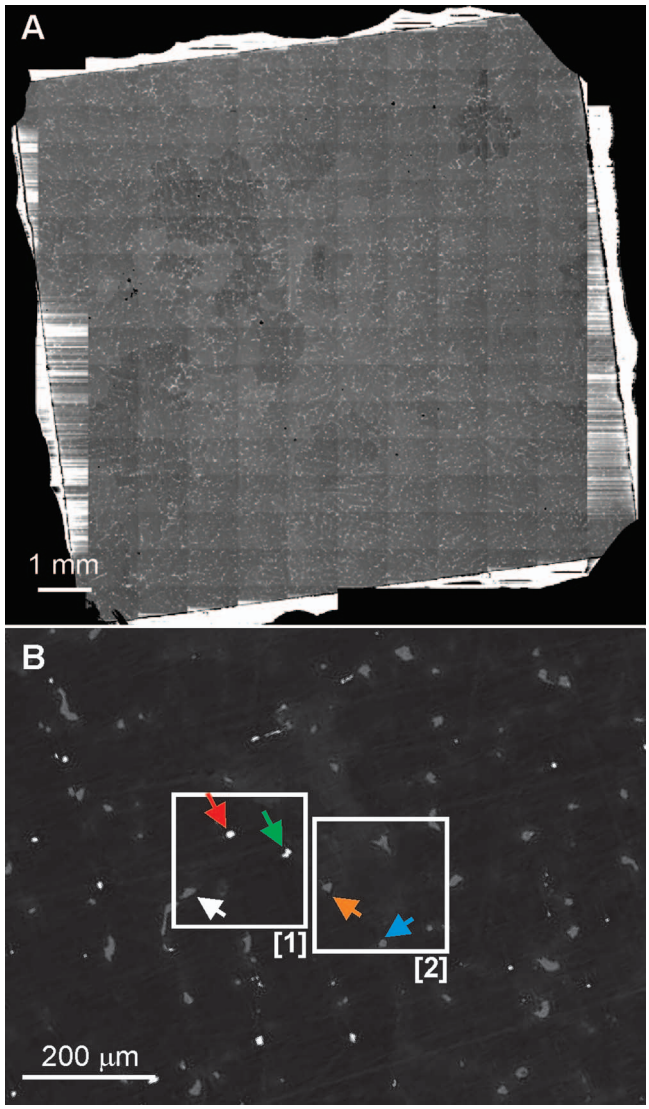

Figure 2. A) 1 × 1 cm montage image of an uncorroded sand cast AM50 Mg alloy: B) SEM micrograph of an area of the alloy surface: AOI [1] and [2] represent two 200 μm × 200 μm areas imaged using SECM in SG/TC mode. Two Al_8Mn_5 particles are marked with red and green arrows and three β-phase locations are marked with orange, blue and white arrows.

CLSM of AOI-1.— As corrosion progresses, the alloy surface topography will change, thus affecting the ME current during the SECM measurement, which is dependent on both the topography and reactivity of the surface.[51] To ensure that the currents measured at the ME are predominantly reactivity based, CLSM was used to evaluate the surface topography of the AOI. Figure 4A shows a CLSM micrograph

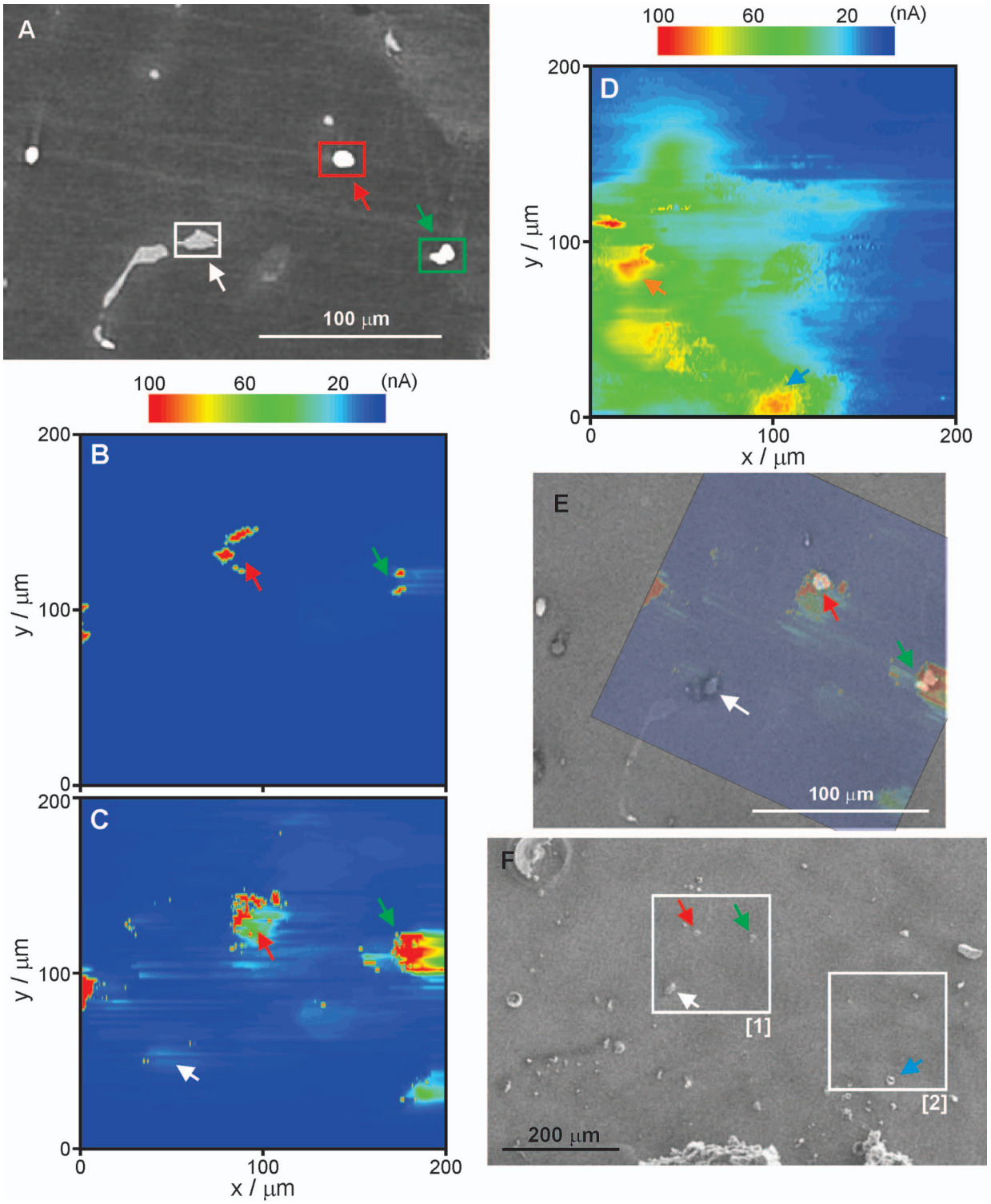

Figure 3. A) Higher magnification SEM micrograph of AOI-1 highlighted in Figure 2B pre corrosion. B) AOI-1 (Figure 3A) of a sand cast AM50 Mg alloy surface imaged using a 25 μm microelectrode tip polarized at −100 mV scanned at 5 μm/s at a tip-to-substrate distance of 10 μm following a 30 minutes exposure time. C) AOI-1 (Figure 3A) imaged after 2 h of immersion. D) AOI-2 (Figure 2B) imaged after 4 h of immersion. Arrows represent features where high H_2 fluxes have been measured in situ. E) Higher magnification SEM micrograph of AOI-1 highlighted in Figure 2B post corrosion (6 h). F) SEM micrograph of the surface post-corrosion (6 h) where AOIs have been identified.

of the alloy surface following corrosion with the location of AOI-1 marked with the white box. A line scan to measure the surface profile was performed across the region marked with a red line. The corresponding surface profile, Figure 4B, shows that the overall depth of corrosion in the α-phase region is ∼3 μm after 6 h of immersion. Since the SECM maps of AOI-1 were recorded after only 30 min and 2 h, the roughness of the mapped surface would be less than this. Additionally, according to theoretical SG/TC expectations, a variation of ∼1.4× the steady-state current is expected for a tip-to-substrate distance of 10 μm.[52] In the present case, a steady-state response of

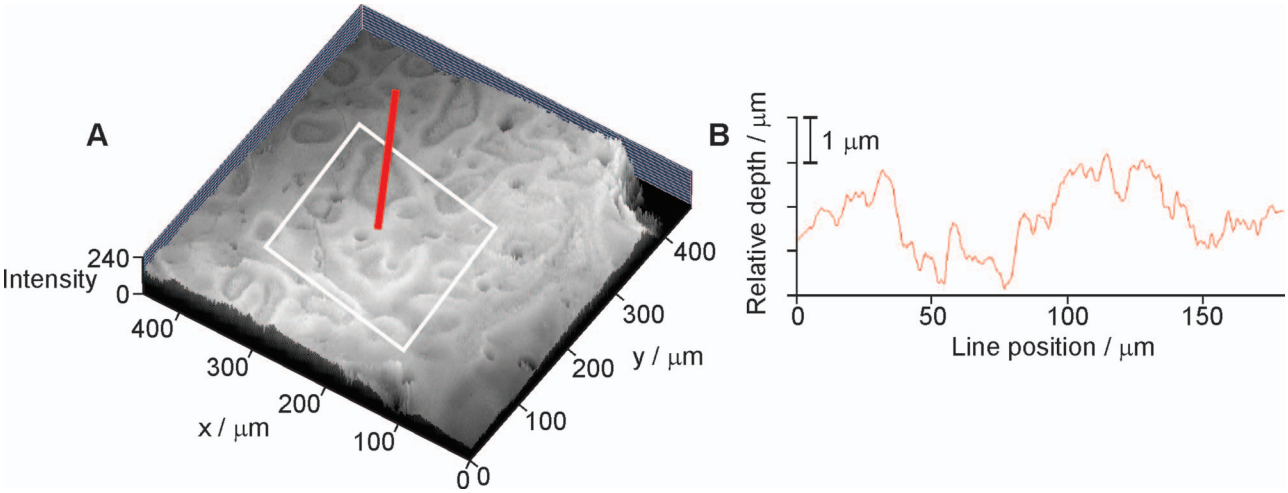

Figure 4. A) CLSM of a 450 μm × 450 μm area, after 6 h of immersion in a 0.016 wt% NaCl solution, with the AOI-1 area highlighted in white post-corrosion. B) Surface height profile measured along the red line in Figure 4A.

2 nA is obtained compared to 100 nA currents recorded over regions liberating H_2. Topography effects are thus minimal in comparison to the recorded current and the local reactivity of the surface dominates the ME current.

Analytical electron microscopy of H_2 evolution sites.— Analytical transmission electron microscopy (TEM) was used to identify the chemical nature of the sites responsible for H_2 evolution. One location that was not scanned by SECM was also analysed for comparison (black frame in Figure 5A). Figure 5A shows the locations and corresponding FIB-prepared TEM specimens at low magnification. The feature marked with a green arrow in Figure 5A, identified to be evolving H_2 after only 30 min of exposure, was selected for analysis. A TEM lamella was extracted using site-specific FIB preparation with a previously reported methodology.[44] The low magnification scanning transmission electron microscopy – high-angle annular dark-field (STEM-HAADF) image of the lamella is presented in Figure 5B, along with a higher magnification of the area marked with the green box shown in Figure 5C. An XEDS analysis of the area outlined in red, Figure 5D, confirmed the region to be a Al_8Mn_5 intermetallic with some Fe content (~2 wt%). The Al concentration in solid solution in the Mg matrix surrounding the intermetallic was around 5–6 wt%, indicating the intermetallic was located in a primary Mg grain, Figure S1. Selected area electron diffraction analysis identified the intermetallic phase to be Al_8Mn_5. The corrosion product dome was predominantly crystalline $Mg(OH)_2$. The above was also observed in the FIB sample prepared from the area marked with a red arrow in Figure 5A.

Another feature selected for TEM analysis was that observed to be evolving H_2 after 2 h immersion marked with a white arrow in Figure 5A. The STEM-HAADF image of the extracted TEM lamella showing a β-phase region is presented in Figure 5E and a higher magnification image in Figure 5F. An XEDS analysis of this region (the area marked in panel F) showed the β-phase to be contaminated with Ni, Figure 5G. The strong Cu signal arises from the sample substrate used to support the FIB-prepared TEM sample.

The combination of SECM mapping and analytical transmission microscopy allowed the locations generating H_2 fluxes in the initial stages of corrosion to be identified and characterized. Initially H_2 was produced at an Al_8Mn_5 intermetallic, containing small amounts of Fe, demonstrating such particles were the initially activated cathodes. These results agree with the previous SKPFM reports showing higher Volta potentials over Al_8Mn_5 intermetallics making them cathodic with respect to the α-Mg matrix.[46] As the immersion time was extended, a β-phase structure contaminated with Ni also became an active cathode, while other non-contaminated β-phase sites remained inactive. Both Fe and Ni are contaminants proven to enhance the corrosion susceptibility of Mg by increasing the reactivity of the cathodes. That these two features should act as cathodes is consistent with their Volta potentials, which are higher than that of the α-Mg matrix.[46] The observation that the Al_8Mn_5 intermetallics served as the main cathodic sites to support corrosion initiation, is contrary to the ex situ observations in atmospheric conditions.[53] As time progressed (for 2 h $< t <$ 6 h), contaminated β-phase activated as the demand for cathodic support by the accelerating corrosion process increased, and possibly also because the accumulation of $Mg(OH)_2$ deposits on the Al_8Mn_5 intermetallics stifled their cathodic reactivity.

As shown by the wide spread green area in Figure 3D, the α-Mg phase also evolved H_2. There appear to be three possible explanations for this: (1) Al-enrichment at the alloy/corrosion product interface as corrosion progressed allowing this area to become cathodic;[44] (2) exposure of cathodic features lying immediately below the polished surface and exposed as corrosion progresses into the alloy; (3) radial diffusion of dissolved H_2 produced at the visible adjacent intermetallic locations. The first two of these possibilities seems unlikely since CLSM, Figure 4, suggested corrosion had not been extensive enough to lead to this enrichment, which has previously been shown to occur on the eutectic regions of this alloy.[44,54] Along those lines, microscopy analysis of FIB samples did not reveal any Al-enrichment of the corrosion product layer.

The SEM and TEM analyses in Figure 5 show that domes of corrosion product (predominantly $Mg(OH)_2$) accumulated above the sites evolving H_2. The domes have been shown to be a fingerprint for cathodic activity at these locations.[50] XEDS analyses of this accumulated product layer, Figure 6A, shown at higher magnification in Figure 6B, revealed that the main elemental components of the dome were Mg, O and C, Figure 6C, as expected from electron diffraction analyses on the prepared samples and previous observations on similar systems.[44] Particles formed within this corrosion product layer exhibited previously unobserved features, Figure 6D. XEDS analyses (Figure 6E) showed these areas (one of which is marked in Figure 6D) were high in Ru (49.91 wt%) and O (19.31 wt%) with some Mg (12.59 wt%). Similar Ru precipitates were far less prevalent over Al_8Mn_5 precipitates not imaged by SECM (area marked with a black frame in Figure 5A and Figure S2) and appeared to form at locations producing high fluxes of H_2. Upon completion of the SECM corrosion experiment, the initially translucent solution was darker and a fine precipitate was observed.

Formation of these Ru particles, including those present within the $Mg(OH)_2$ corrosion product dome, occurred in a similar manner to the formation of $Mg(OH)_2$; i.e., as a consequence of the rise in alkalinity

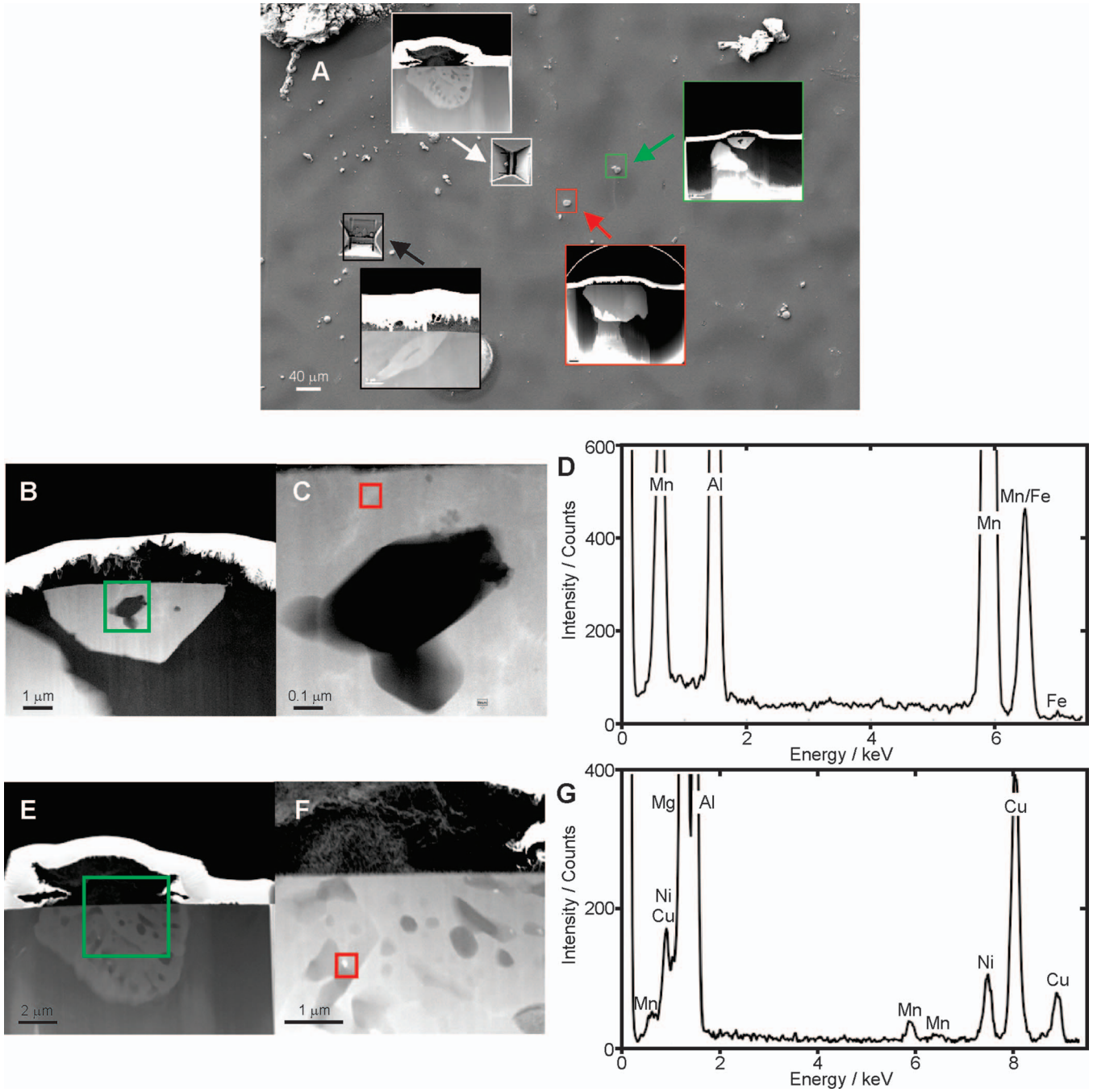

Figure 5. Post-corrosion TEM and XEDS analysis. A) Locations and the final FIB-prepared TEM specimens marked on the as-corroded alloy surface. The area marked with the black frame is an area not scanned by SECM and was prepared for comparison (Figure S2). B) STEM-HAADF micrograph of the FIB lamella lifted from the surface post-corrosion. This sample was extracted from the area highlighted by the green arrow in Figure 5A. C) Higher magnification image of marked area (green frame) in Figure 5B. D) XEDS data from the location framed in Figure 5C. E) STEM-HAADF micrograph of the FIB lamella lifted from the surface post-corrosion. This sample was extracted from the area highlighted by the white arrow in Figure 5A. F) Higher magnification image of marked area (green frame) in Figure 5E. G) XEDS data from the location framed in Figure 5F.

caused by water reduction. The Ru in the $Ru(NH_3)_6Cl_3$ solution is also insoluble at higher pH values, and observed to form a black precipitate after 6 h of contact with corroding Mg. A similar black precipitate has been observed to form in alkaline solutions and was reported to be $Ru(OH)_3$.[55] The nature of the precipitate in our solution was confirmed by elemental analysis (EA), thermal gravimetric analysis (TGA) and infrared spectroscopy (IR), as shown in the supplementary data, Figure S3 – Figure S5.

Electrochemical analyses showed a loss of electrochemical response over time in a solution of 1 mM $Ru(NH_3)_6Cl_3$ at pH = 12.98 as a black precipitate was formed. This precipitate was extracted and isolated from the solution and IR analysis identified the presence of peaks for the N-H stretching mode. TGA and EA analyses then identified the precipitate as a Ru based partially de-aminated complex, $Ru^{IV}(NH_3)O_2$. The $Ru^{IV}(NH_3)O_2$ is insoluble at high pH (~13) and can co-precipitate with $Mg(OH)_2$ at locations supporting water reduction. This would account for the detection of Ru in the corrosion product layer, Figure 6. RuAg particles were also observed, expected to arise from loss of Ag from the non-fritted reference electrode and depositing in a similar fashion to the Ru particle. Therefore,

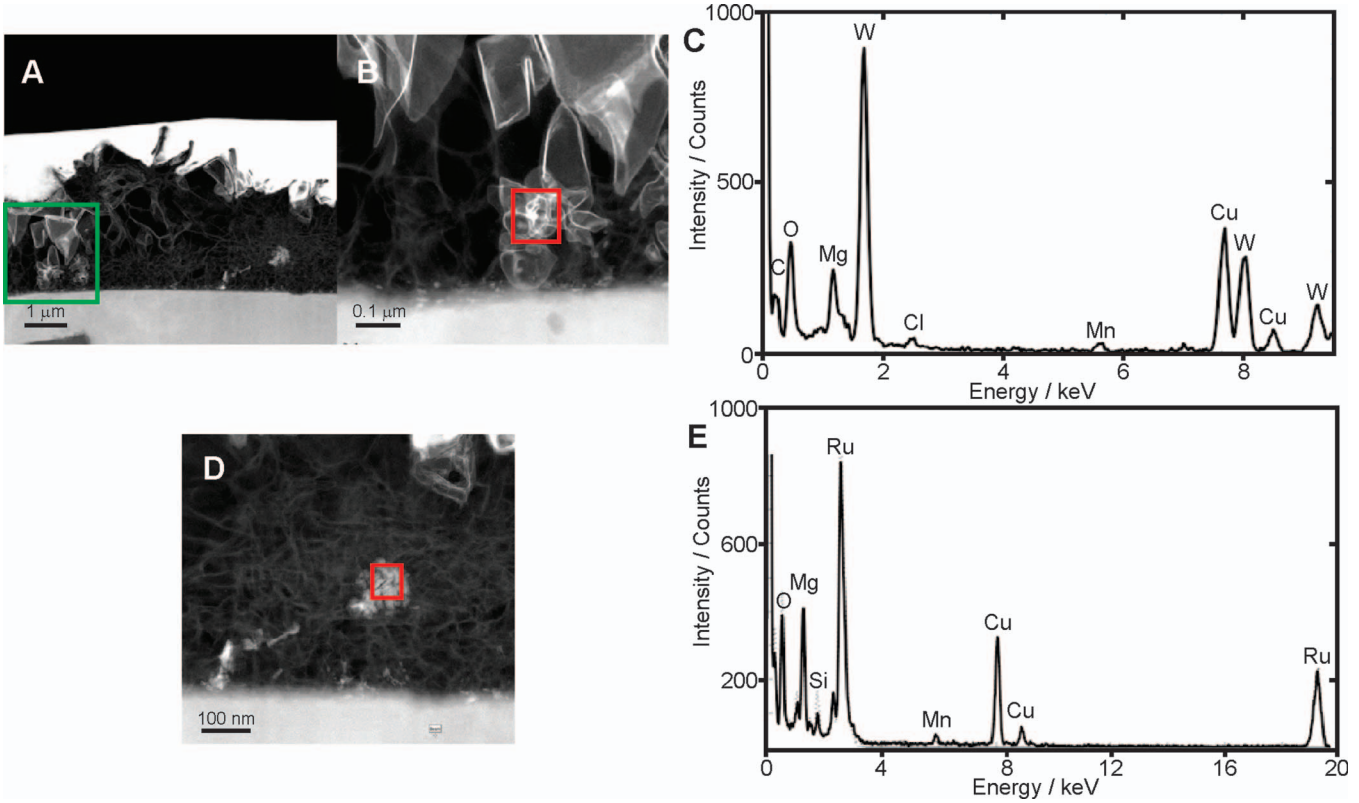

Figure 6. A) High magnification STEM-HAADF micrograph of the corrosion product layer shown in Figure 5A. B) Higher magnification image of the area within the green frame in Figure 6A. C) XEDS data from the location framed in Figure 6B. D) High magnification STEM-HAADF micrograph of the corrosion product layer. E) XEDS data from the location framed in Figure 6D.

$Ru(NH_3)_6Cl_3$, thought to be a stable redox mediator, was found to be a pH sensitive redox probe that precipitates over high pH regions (~13) during corrosion of the alloy.

Conclusions

A combination of surface characterization, in situ SECM mapping and analytical transmission electron microscopy were successfully employed to monitor the initial stages of corrosion of a sand-cast AM50 Mg alloy. Using the SG/TC mode of SECM, the flux of molecular H_2 from microgalvanically coupled cathodic microstructures at the Mg alloy interface was imaged. Cross-correlation of the locations of H_2 production with SEM micrographs demonstrated that the initial H_2 evolution occurred at Al_8Mn_5 intermetallics with evolution on β-phase structures observed after 2 h of immersion. XEDS analyses performed on TEM samples extracted from the SECM active regions revealed contamination with Fe (Al_8Mn_5 intermetallic precipitate) and Ni (β-phase intermetallic), indicating that the presence of these cathodically active contaminants enhances the alloy corrosion susceptibility. This tandem electron and electrochemical microscopies methodology can be extended to detect and investigate cathode locations on the surface of other Mg alloys. The combined information of the local morphology, chemical composition and electrochemical activity of the different microstructure components is required for the further development of predictive 3D SECM numerical models applied to corrosion.

Acknowledgments

The authors acknowledge funding by General Motors Canada and the Natural Sciences and Engineering Research Council of Canada (NSERC, 140577928). Igor Huskic and Dr. Tomislav Friscic from McGill University are acknowledged for their help with the Ru precipitate characterization. The TEM characterization was carried out at the Canadian Centre for Electron Microscopy, a facility supported by NSERC and McMaster University. We thank the staff at Integrated Microscopy at the Biotron and ZAPLab at Western University for instrumentation access.

References

1. C. H. Caceres, *Metall and Mat Trans A*, **38**, 1649 (2007).
2. M. Hakamada, T. Furuta, Y. Chino, Y. Chen, H. Kusuda, and M. Mabuchi, *Energy*, **32**, 1352 (2007).
3. S. Maddela, Y. M. Wang, A. K. Sachdev, and R. Balasubramaniam, *Magnesium Technology*, 321 (2009).
4. C. H. Cáceres, *Materials & Design*, **30**, 2813 (2009).
5. R. A. Witik, J. Payet, V. Michaud, C. Ludwig, and J.-A. E. Månson, *Composites Part A: Applied Science and Manufacturing*, **42**, 1694 (2011).
6. Z. Shi, M. Liu, and A. Atrens, *Corros. Sci.*, **52**, 579 (2010).
7. G. Song and A. Atrens, *Adv. Eng. Mater.*, **9**, 177 (2007).
8. G. Song, *Adv. Eng. Mater.*, **7**, 563 (2005).
9. K. B. Deshpande, *Corros. Sci.*, **52**, 3514 (2010).
10. R. Ambat, N. N. Aung, and W. Zhou, *Corros. Sci.*, **42**, 1433 (2000).
11. G. Song, A. L. Bowles, and D. H. StJohn, *Materials Science and Engineering: A*, **366**, 74 (2004).
12. M.-C. Zhao, M. Liu, G. Song, and A. Atrens, *Corros. Sci.*, **50**, 1939 (2008).
13. A. Davoodi, J. Pan, C. Leygraf, R. Parvizi, and S. Norgren, *Mater. Corros.*, **64**, 195 (2013).
14. X. Liu, T. Zhang, Y. Shao, G. Meng, and F. Wang, *Mater. Corros.*, **63**, 505 (2012).
15. W. Liu, F. Cao, Y. Xia, L. Chang, and J. Zhang, *Electrochim. Acta*, **132**, 377 (2014).
16. R. M. Souto, A. Kiss, J. Izquierdo, L. Nagy, I. Bitter, and G. Nagy, *Electrochem. Commun.*, **26**, 25 (2013).
17. S. S. Jamali, S. E. Moulton, D. E. Tallman, M. Forsyth, J. Weber, and G. G. Wallace, *Corros. Sci.*, (2014).
18. S. V. Lamaka, O. V. Karavai, A. C. Bastos, M. L. Zheludkevich, and M. G. S. Ferreira, *Electrochem. Commun.*, **10**, 259 (2008).
19. S. V. Lamaka, G. Knörnschild, D. V. Snihirova, M. G. Taryba, M. L. Zheludkevich, and M. G. S. Ferreira, *Electrochim. Acta*, **55**, 131 (2009).
20. A. J. López, C. Taltavull, B. Torres, E. Otero, and J. Rams, *Corrosion*, **69**, 497 (2013).
21. G.-L. Song and Z. Xu, *Corros. Sci.*, **63**, 100 (2012).

22. F. Andreatta, I. Apachitei, A. A. Kodentsov, J. Dzwonczyk, and J. Duszczyk, *Electrochim. Acta*, **51**, 3551 (2006).
23. D. Trinh, P. Dauphin Ducharme, U. Mengesha Tefashe, J. R. Kish, and J. Mauzeroll, *Anal. Chem.*, **84**, 9899 (2012).
24. K. B. Deshpande, *Corros. Sci.*, **52**, 2819 (2010).
25. G. Williams and H. Neil McMurray, *J. Electrochem. Soc.*, **155**, C340 (2008).
26. G. Galicia, N. Pébère, B. Tribollet, and V. Vivier, *Corros. Sci.*, **51**, 1789 (2009).
27. A. J. Bard, F.-R. F. Fan, J. Kwak, and O. Lev, *Anal. Chem.*, **61**, 132 (1989).
28. S. B. Basame and H. S. White, *J. Phys. Chem. B*, **102**, 9812 (1998).
29. L. F. Garfias-Mesias, M. Alodan, P. I. James, and W. H. Smyri, *J. Electrochem. Soc.*, **145**, 2005 (1998).
30. Y. González-García, J. J. Santana, J. González-Guzmán, J. Izquierdo, S. González, and R. M. Souto, *Prog. Org. Coat.*, **69**, 110 (2010).
31. H. He, R. K. Zhu, Z. Qin, P. Keech, Z. Ding, and D. W. Shoesmith, *J. Electrochem. Soc.*, **156**, C87 (2009).
32. A. C. Bastos, A. M. Simões, S. González, Y. González-García, and R. M. Souto, *Prog. Org. Coat.*, **53**, 177 (2005).
33. J. Izquierdo, L. Nagy, I. Bitter, R. M. Souto, and G. Nagy, *Electrochim. Acta*, **87**, 283 (2013).
34. O. V. Karavai, A. C. Bastos, M. L. Zheludkevich, M. G. Taryba, S. V. Lamaka, and M. G. S. Ferreira, *Electrochim. Acta*, **55**, 5401 (2010).
35. J. Izquierdo, A. Kiss, J. J. Santana, L. Nagy, I. Bitter, H. S. Isaacs, G. Nagy, and R. M. Souto, *J. Electrochem. Soc.*, **160**, C451 (2013).
36. G. S. Frankel, A. Samaniego, and N. Birbilis, *Corros. Sci.*, **70**, 104 (2013).
37. D. R. Lide, *CRC Handbook of Chemistry and Physics*, 94th Edition, Taylor & Francis, (2013).
38. K. C. Leonard and A. J. Bard, *J. Am. Chem. Soc.*, **135**, 15890 (2013).
39. K. Fushimi, K. A. Lill, and H. Habazaki, *Electrochim. Acta*, **52**, 4246 (2007).
40. U. M. Tefashe, M. E. Snowden, P. Ducharme Dauphin, M. Danaie, G. A. Botton, and J. Mauzeroll, *J. Electroanal. Chem.*, **720–721**, 121 (2014).
41. C. Nowierski, J. J. Noël, D. W. Shoesmith, and Z. Ding, *Electrochem. Commun.*, **11**, 1234 (2009).
42. M. A. Mezour, M. Morin, and J. Mauzeroll, *Anal. Chem.*, **83**, 2378 (2011).
43. T .J. Smith and K. J. Stevenson, 4 - Reference Electrodes, in: C. G. Zoski (Ed.) *Handbook of Electrochemistry*, Elsevier, Amsterdam, (2007), pp. 73–110.
44. M. Danaie, R. M. Asmussen, P. Jakupi, D. W. Shoesmith, and G. A. Botton, *Corros. Sci.*, **77**, 151 (2013).
45. J. Hirsch and T. Al-Samman, *Acta Mater.*, **61**, 818 (2013).
46. M. Jönsson, D. Thierry, and N. LeBozec, *Corros. Sci.*, **48**, 1193 (2006).
47. S. Mathieu, C. Rapin, J. Steinmetz, and P. Steinmetz, *Corros. Sci.*, **45**, 2741 (2003).
48. A. Pardo, M. C. Merino, A. E. Coy, R. Arrabal, F. Viejo, and E. Matykina, *Corros. Sci.*, **50**, 823 (2008).
49. R.-c. Zeng, J. Zhang, W.-j. Huang, W. Dietzel, K. U. Kainer, C. Blawert, and W. Ke, *Transactions of Nonferrous Metals Society of China*, **16**(Supplement 2), s763 (2006).
50. M. Danaie, R. M. Asmussen, P. Jakupi, D. W. Shoesmith, and G. A. Botton, *Corros. Sci.*, **83**, 299 (2014).
51. P. Sun, F. O. Laforge, and M. V. Mirkin, *PCCP*, **9**, 802 (2007).
52. R. D. Martin and P. R. Unwin, *Anal. Chem.*, **70**, 276 (1998).
53. M. Jönsson, D. Persson, and R. Gubner, *J. Electrochem. Soc.*, **154**, C684 (2007).
54. R. Matthew Asmussen, W. Jeffrey Binns, P. Jakupi, and D. Shoesmith, *J. Electrochem. Soc.*, **161**, C501 (2014).
55. D. Bhattarai, J.-h. Lee, and G. Keum, Ruthenium hydroxide, in: *Encyclopedia of Reagents for Organic Synthesis*, John Wiley & Sons, Ltd, (2001).